Interlayer exciton landscape in WS$_2$/tetracene heterostructures

Interlayer exciton landscape in WS$_2$/tetracene heterostructures

Joshua J. P. Thompson,[1] Victoria Lumsargis,[2] Maja Feierabend,[3] Quichen Zhao,[2,4] Kang Wang,[5] Letian Dou,[5] Libai Huang,[2] and Ermin Malic[1,3]

[1]*Department of Physics, Philipps-Universität Marburg, 35037 Marburg, Germany*[*]
[2]*Department of Chemistry, Purdue University, West Lafayette, Indiana, 47907, United States*
[3]*Department of Physics, Chalmers University of Technology, 412 96 Gothenburg, Sweden*
[4]*State Key Laboratory of Superhard Materials, Jilin University, Changchun, Jilin, 130012, China*
[5]*Davidson School of Chemical Engineering, Purdue University, West Lafayette, Indiana, 47907, United States*

The vertical stacking of two-dimensional materials into heterostructures gives rise to a plethora of intriguing optoelectronic properties and presents an unprecedented potential for technological development. While much progress has been made combining different monolayers of transition metal dichalgonenides (TMDs), little is known about TMD-based heterostructures including organic layers of molecules. Here, we present a joint theory-experiment study on a TMD/tetracene heterostructure demonstrating clear signatures of spatially separated interlayer excitons in low temperature photoluminescence spectra. Here, the Coulomb-bound electrons and holes are localized either in the TMD or in the molecule layer, respectively. We reveal both in theory and experiment signatures of the entire intra- and interlayer exciton landscape in the photoluminescence spectra. In particular, we find both in theory and experiment a pronounced transfer of intensity from the intralayer TMD exciton to a series of energetically lower interlayer excitons with decreasing temperature. In addition, we find signatures of phonon-sidebands stemming from these interlayer exciton states. Our findings shed light on the microscopic nature of interlayer excitons in TMD/molecule heterostructures and could have important implications for technological applications of these materials.

A controlled vertical stacking of atomically thin materials into van der Waals heterostructures with tailored properties has recently become feasible[1,2]. In particular, there has been much progress in understanding homo- and heterobilayers of transition metal dichalcogenides (TMDs)[3–8]. The strong Coulomb interaction leads to a variety of excitons in these materials[9–13]. Recent experiments have observed signatures of spatially separated interlayer exciton states (ILXs)[6,14–16]. So far, ILX signatures have been mostly demonstrated in TMD homo- and heterobilayers. A recent study showed that ILXs can also be observed in organic/heterostructures, where a thin crystalline film of organic molecules is stacked on a TMD monolayer[17]. Tetracene (Tc) molecules are of particular interest due to their excellent light-emitting and light-harvesting properties[18–20] and their similar band gap energies to TMD materials[21].

Interfaces of TMDs and organic molecules have recently attracted significant interest[22–24]. This is in part due to the complimentary properties of the two systems. TMDs possess large electronic mobilities[25] and are regularly used in optoelectronic applications. In contrast, molecular films such as Tc have a low mobility, yet have many advantages over TMDs in optoelectronic applications. These include high optical absorption efficiency[17]; low-cost fabrication[23]; singlet fission, allowing efficient energy transfer in photovoltaics[26]; and regioselective modification, which permits the fine tuning of the electronic and optical properties of the molecule[27]. These, coupled with the relatively enormous family of organic molecules compared to that of TMDs offers an almost infinite playground with which to tailor devices. A detailed understanding of the electronic and optical properties of such interfaces is therefore paramount. In particular the behaviour of excitons at this interface crucially determines the properties and functionality of photovoltaic and other optical applications including sensors.
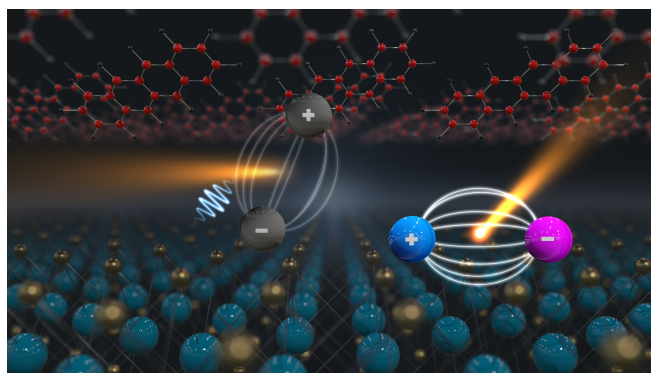

Figure 1. **Artistic illustration of intra- and interlayer excitons in a TMD/Tc heterostructure.** Intralayer exciton (coloured) can efficiently emit light, while interlayer excitons (grey) show a much lower oscillator strength. However, driven by scattering with phonons (blue wave) their occupation can exceed the one of bright exciton by order of magnitude making them visible in low-temperature PL spectra.

After optical excitation of an intralayer exciton in the TMD layer, efficient charge transfer enables the hole to tunnel from the TMD to the organic layer, while still being attracted to the TMD electron (cf. Fig. 1). The spatially separated electron-hole pair is an interlayer exciton (also known as charge transfer or hybrid exciton). Due to their spatial separation, ILXs in van der Waals heterostructures have a small oscillator strength and are thus in general darker than intralayer excitons (illustrated with the grey ILX in Fig. 1). While there is increasing number of studies on ILX signatures in PL spectra in TMD bilayers[6,28], little is known about the intra- and interlayer exciton landscape and their optical spectra characterizing TMD/molecule heterostructures. In this work, we undertake a joint theory-experiment study to uncover the temperature dependent excitonic signatures of a tungsten disul-

fide (WS$_2$)/Tc heterostructure as an exemplary system for the broad class of TMD/molecule heterostructures.

To obtain microscopic insights, we apply a quantum-mechanical approach based on the density matrix formalism[29,30]. In particular, we solve the Wannier equation allowing us to microscopically resolve the entire intra- and interlayer exciton landscape in the investigated materials including binding energies and wave functions. Solving the generalized Elliott formula we also have microscopic access to their optical signatures[31,32]. Experimentally, we perform temperature-dependent photoluminescence (PL) measurements on WS$_2$/Tc heterostructures and demonstrate the appearance of ILXs at energies well below the optically excited intralayer exciton. In excellent agreement with theoretical predictions, we show how the ILX intensity significantly increases at lower temperatures. We find that these signatures are composed of two close-lying ILXs originating from two distinct electronic valleys in the TMD layer, reflecting the complex ILX landscape of TMDs. Furthermore, we demonstrate both in experiment and theory signatures of ILX phonon sidebands. The latter are identified as a low-energy shoulder of the ILX resonance. Overall, our work provides new microscopic insights into the intriguing ILX landscape and the resulting optical response in technologically promising organic/inorganic heterostructures.

Interlayer exciton landscape. We focus on heterostructures comprising of a WS$_2$ monolayer and a thin crystalline film of Tc molecules. The latter attach to the surface of the TMD via van der Waals bonds and form a molecular lattice, as has been shown in previous studies[33,34]. Tetracene molecules tend to form periodic lattices rather than distribute randomly on the surface[35–39]. Motivated by these findings, we describe the Tc layer as a quasi two-dimensional structure characterized by a HOMO-LUMO gap. We take into account one state in the conduction and valence band denoted as l (lowest unoccupied molecular orbital) and h (highest occupied molecular orbital). This is justified since the bandwidth of the l and h bands in the molecular layer is very small compared to the TMD conduction and valence bands[40–42]. Hence, the number of observed ILXs will be primarily determined by the TMD band structure cf. Fig. 2. The molecular states, while slightly dispersive, have a quasi-flat dispersion, cf. Fig. 2 owing to the relatively weak hopping between molecules[42–44]. Due to their relative band alignment[45,46], Tc and WS$_2$ form a type-II heterostructure[17] in contrast to, for example, Tc and molybdenum-based TMDs which form type-I heterostructures[24] and hence do not facilitate the formation of optically-active interlayer excitons. As a result, WS$_2$/Tc represents an exemplary system, playing host to interlayer excitons[17] as well as a rich substructure of intralayer dark states in the WS$_2$[31,47,48].

To describe the TMD/Tc heterostructure on a microscopic level, we use the density matrix formalism[29,30,32,49,50]. For the TMD, we take into account the band structure around the high-symmetry points in the reciprocal space within an effective mass approximation[51]. In particular, we consider the valence band maxima at the K point and conduction band min-

ima at the K,Λ, and K' valley, which are crucial in determining the exciton landscape[10]. Depending on the location of the electron and hole, we can distinguish different intralayer KK, KΛ and KK' excitons (yellow/orange ovals in Fig. 2) and molecular excitons hl (black oval in Fig. 2). Furthermore, due to the type-II band alignment[17] there are lower lying spatially separated interlayer excitons hK, hΛ, hK', combining electrons in the WS$_2$ layer and holes on the molecular layer (blue ovals in Fig. 2) as well as a higher energy interlayer exciton with the electron and hole located on opposite layers, Kl (oval omitted for clarity). The energy values determining the band alignment with respect to the vacuum level are obtained from the literature[45,46,52]. Here, the first/second letter describes the position of the hole/electron, e.g. the state hK corresponds to the hole located in the h state of the molecule, while the electron can be found in the K valley of the TMD layer, cf. Fig. 2(a). The quasi-flatness of the molecular dispersion means that ILXs are spread over a larger area of momentum-space, reflecting its real space localisation. Furthermore, since the Brillouin zones of WS$_2$ and Tc layers are considerably different, we assume that all ILXs are bright as no momentum transfer is required[53].

As excitonic effects are crucial in TMDs[49,54–56], we project our equations into an excitonic basis with eigenenergies ϵ_μ and wave functions φ_q^μ. Note that the index μ can include both intralayer μ =(KK,KΛ,KK',hl) and interlayer states μ =(hK,hΛ,hK',Kl). The excitonic eigenfunctions and eigenenergies are obtained by solving the Wannier equation[29,30,49]. The Coulomb matrix element is calculated using an effective 2D Coulomb potential $V_k^\mu = \frac{e_0^2}{k\epsilon_0\epsilon(k)}$ with the dielectric function $\epsilon(k)$ depending on the screening of the two layers $\epsilon^{\text{TMD}}/\epsilon^{\text{Tc}}$, the screening of the surrounding material ϵ^{sur}, the thickness of the layers $d^{\text{TMD}}/d^{\text{Tc}}$ and the interlayer distance $d^{\text{TMD-Tc}}$. Further details on the derivation of the dielectric function can be found in Ref. 27. Table S1 in the supplementary information summarizes the parameters used in our study. The assumed thickness of the molecular film corresponds to a single layer of molecules in an upright configuration[17,22]. Note that in experimental setups, the molecular layer of $\sim$ 20 nm consists of more than one layer, however, we assume that the main interaction and charge transfer takes place within the first layer. This is further justified since in ab-initio calculations, exciton wavefunctions in organic semiconductors exist primarily within single layer planes[43]. Solving the Wannier equation, we obtain the binding energies of the entire exciton landscape including bright and dark intra- and interlayer excitons, as illustrated in Figure 2(b). While momentum-dark and bright intralayer excitons are easily defined, the precise nature of ILXs is harder to pin down. Changes in the growth conditions and substrate quality alter the structure of the molecular lattice and hence its dispersion, however, as already stated, the significant lattice mismatch and the large momentum spread of the molecular hole in the ILXs allows this bright/dark dichotomy to be neglected.

For WS$_2$/Tc heterostructures on a Si/SiO$_2$ substrate, we find an exciton binding energy of 196 meV for the intralayer exciton within the WS$_2$ layer. Furthermore, we find binding energies of 243 meV and 272 meV for the two bright hK
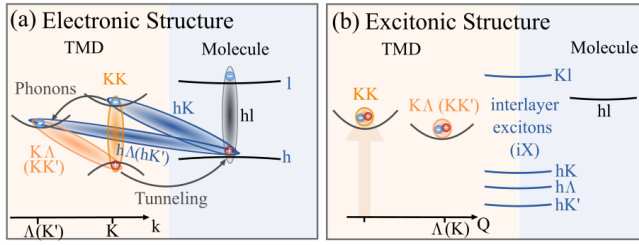
Figure 2. **Bandstructure of intra- and interlayer excitons.** (a) Electronic dispersion of a WS_2 monolayer around the high symmetry K and Λ (K') points and the homo-lumo gap in Tc molecules. (b) Excitonic dispersion of the WS_2/Tc heterostructure including intra- and interlayer states obtained from the solution of the Wannier equation.

and Kl interlayer exciton states, respectively. Although counter-intuitive at first glance, the larger binding energy in the ILX state comes from the larger effective mass of the hole in the molecular layer. The ILX has a larger binding energy of 328 (272) meV reflecting the larger effective mass at the Λ (K') point. The binding energies are slightly lower then for intralayer excitons in the WS_2 monolayer due to the larger dielectric screening within a heterostructure. The energies are in a similar range as values reported for TMD/TMD heterostructures[6,7,28]. While the large effective masses and smaller dielectric screening in the molecular film lead to heavier excitons and hence enlarged binding energies, the relatively large thickness of the molecular layer compared to the TMD monolayer reduces the exciton binding energy. Note that the energies discussed so far are pure binding energies E_μ^b. For the absolute spectral position E_μ of excitons (shown in Fig. 2(b)), one needs to take into account the band gap energy E_μ^g with $E_\mu = E_\mu^g - E_\mu^b$. We shifted the whole exciton landscape to match the experimentally measured A exciton resonance at 2.0 eV. Overall, we find that the interlayer hK' exciton is the energetically lowest state, followed by $E_{h\Lambda}$ and E_{hK}, cf. Fig. 2(b) and Table S1. The interlayer Kl exciton is located 1.1 eV above the bright KK exciton and thus has no influence on PL spectra and will be neglected in the following. Moreover, we do not consider the intralayer molecule state hl (located at 2.56 eV), since our focus lies on optical excitation resonant to the energetically lower intralayer TMD exciton. For simplicity we consider only one spin in this study. Owing to the spin degeneracy of the Tc, for spin-bright excitons (same-spin), we find that hK ($\uparrow\uparrow$) = hK'($\downarrow\downarrow$) and hK' ($\uparrow\uparrow$) = hK($\downarrow\downarrow$) eliminating the need to consider spins separately in our analysis. Spin-dark excitons (opposite spins) are not optically active and can be neglected.

Interlayer excitons in photoluminescence. After determining the exciton landscape in WS_2/Tc heterostructures, we focus now on their optical response in PL spectra. The important (fixed) input parameters (effective masses, band gap energies) are obtained from DFT calculations for the electronic bandstructure[40,51], cf. Table S1 in the supplementary information. We exploit the equation of motion for the photon-
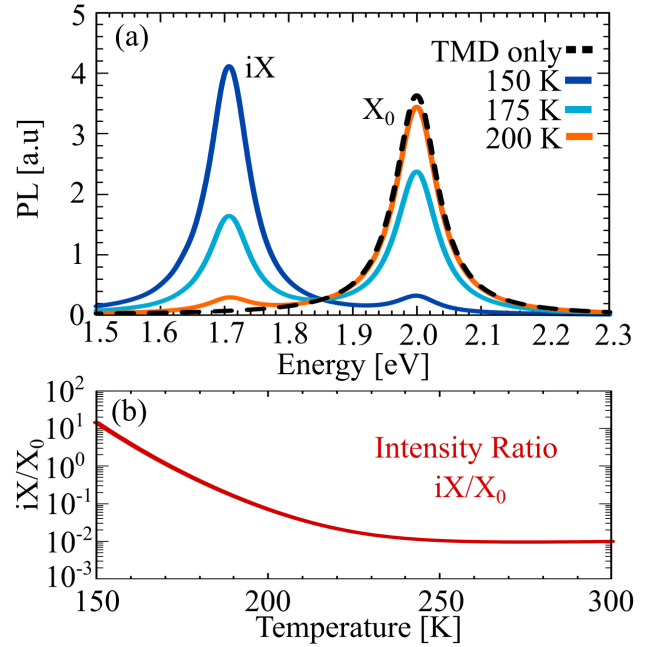

Figure 3. **Optical signature of interlayer excitons.** (a) Calculated PL spectrum of a WS_2/Tc heterostructure on a $Si-SiO_2$ substrate illustrating the drastically growing intensity of the hK' interlayer exciton resonance for reduced temperatures. For comparison, the calculated PL for a WS_2 monolayer at 200 K is shown with the dashed line exhibiting only the intralayer exciton resonance. (b) The intensity ratio between the hK' interlayer (iX) and KK intralayer excitons (X_0), plotted on a log scale.

assisted polarization to obtain the PL intensity I_{PL} for intra- and interlayer excitons resulting in the Elliott formula[31]

$$I_{\mathrm{PL}}(\omega, T) \propto \sum_{\mu = \mathrm{KK,hK}} \frac{|M_\mu|^2 \gamma_\mu N_\mu(T)}{(E_\mu - \omega)^2 + (\gamma_\mu + \Gamma_\mu(T))^2}, \quad (1)$$

where the position of the resonances is given by the energy E_μ, the resonance width by the radiative (γ_μ) and the non-radiative phonon-assisted ($\Gamma_\mu(T)$) dephasing, and finally the oscillator strength by the exciton-photon matrix element $M_\mu = \delta_{Q,0} \sum_q \varphi_q^\mu M_q^\mu \hat{U}_\mu$. The latter is determined by the exciton wave function φ_q^μ, the momentum-dependent optical matrix element[49] M_q^μ and the transformation matrix $\hat{U}_\mu$ which includes the tunneling. The Kronecker-delta ensures that only bright excitons within the light cone with $Q = 0$ are optically active[31]. The appearing exciton occupation $N_\mu(T)$ is crucial in determining the spectral weight of different transitions in the PL spectrum. In this study, we assume thermalized Boltzmann distributions $N_\mu(T) \propto \exp\left(-E_\mu/k_B T\right)$, since we discuss the stationary PL only[31,32]. More details on the origin of Eq. 1 can be found in the supplementary information.

Evaluating Eq. (1) numerically, we investigate optical signatures of intra- and interlayer excitons in the WS_2/Tc heterostructure. The PL spectrum at large temperature (>200 K) exhibits a pronounced resonance at 2 eV stemming from the bright intralayer KK exciton, cf. Fig. 3(a). As the

temperature decreases we observe the emergence of a second peak around 1.71 eV that corresponds to the expected position of the ILX. Further lowering the temperature increases the ratio between the inter- and intralayer exciton peaks (cf. Fig 3 (b)) until at low temperatures (<150 K) the intralayer contributions becomes negligible and the PL spectrum is entirely dominated by ILXs. The lower the temperature, the higher the occupation of the energetically lower-lying ILX states which leads to a more intense ILX resonance in the PL spectra. Therefore, the temperature acts as an externally accessible knob allowing the relative visibility of ILXs to be tuned. Figure 3 (b) shows the temperature-dependent intensity ratio of inter- and intralayer excitons on a logarithmic scale, which resembles the Boltzmann distribution. The ILX in TMD/Tc heterostructures is visible at higher temperatures than in TMD bilayers. The main reason is that the interlayer hK' exciton is about 20 meV lower in energy than the corresponding ILX states in TMD bilayers[7,14–16,28]. This leads to a higher occupation N_μ in equilibrium and thus to the stronger ILX contribution, cf. Eq. (1). Note that we have neglected temperature-induced spectral shifts, linewidth changes and possible modifications in the molecular layer, since they are not expected to have an impact on the qualitative temperature trend of PL intensity ratios.

Signatures of ILX phonon-sidebands. So far, we have focused on direct ILX emission, however we know from TMD monolayers that intralayer excitons show pronounced signatures via phonon-assisted indirect emission resulting in phonon sidebands[31,57,58]. In TMD homo- and heterobilayers, indirect, phonon-assisted signatures of dark interlayer excitons have been observed[7,16,53,59]. To account for these indirect emission channels also for ILX states, we exploit a generalized Elliott formula[31]

$$I_{\mathrm{PL}}(\omega, T) \propto \sum_{\substack{\nu\mu \\ Q, \alpha\pm}} \frac{\Theta^\nu(\omega, T)|D_{Q\alpha}^{\nu\mu}|^2 \Gamma_\mu(T) N_\mu(T) \eta_\alpha^\pm(T)}{(E_\mu \pm \Omega_Q^\alpha - \omega)^2 + (\Gamma_\mu(T))^2}$$

(2)

with $\Theta^\nu(\omega, T) = \frac{|M^\nu|^2}{(E_\nu - \omega)^2 + (\gamma^\nu + \Gamma^\nu(T))^2}$. We take into account all ILX states $\nu = (KK, K\Lambda, KK', hK, h\Lambda, hK')$. The position of resonances is determined by the energy of the corresponding exciton E_μ plus/minus the energy of the absorbed/emitted phonon $\pm\Omega_Q^\alpha$ in the mode α. We account for longitudinal and transversal optical and acoustic phonon modes. The temperature dependent phonon occupation n_α^{ph} enters in $\eta_\alpha^\pm(T) = \left(\frac{1}{2} \mp \frac{1}{2} + n_\alpha^{\mathrm{ph}}(T)\right)$ corresponding to a Bose distribution (bath approximation[60]). In contrast to direct emission, phonon-sidebands cannot decay radiatively[61], hence their spectral width is only determined by non-radiative dephasing Γ_μ[31,32,61]. The oscillator strength of phonon-assisted indirect emission scales with the exciton-phonon scattering element $|D_{Q\alpha}^{\nu\mu}|^2 = \sum_q \varphi_q^\mu g_Q^{\nu\mu} \varphi_{q+\alpha Q}^\nu$, where $g_Q^{\nu\mu}$ is the electron-phonon coupling element[31,32].

Evaluating Eqs. (1) and (2), we calculate the temperature-dependent PL including direct and indirect phonon-assisted emission from excitons in the investigated WS$_2$/Tc het-
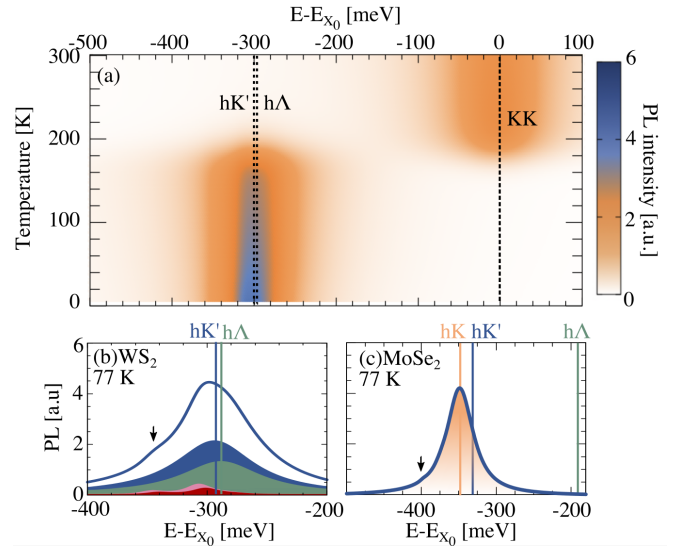

Figure 4. **Fine structure of interlayer excitons.** (a) Calculated temperature-dependent PL of WS$_2$/Tc heterostructure exhibiting signatures from intra- and interlayer excitons. Note that the origin of the energy axis has been shifted to the position of the bright KK exciton (E_{X_0}). (b) Constant temperature cut outlining the contributions of the phonon-assisted indirect PL from interlayer exciton hK' and hΛ. The zero phonon peak contribution is shown in shaded-blue (green), while the phonon-sideband contributions are pink (red) for the hK' (hΛ) excitons. (c) For comparison, we also show the low-temperature PL for MoSe$_2$ exhibiting less significant phonon sidebands.

erostructure, cf. Fig. 4(a). We find that at room temperature the PL is dominated by the direct KK exciton X_0, while the interlayer excitons (hK'/hΛ) located approximately 300 meV below X_0 becomes dominant in the temperature range below 200 K. At very low temperatures new resonances at lower energies appear and can be assigned to phonon-assisted emission from interlayer hΛ and hK' excitons, respectively. To better understand these phonon sidebands, we zoom into the low-energy ILX contribution at 77 K, cf. Fig. 4(b). We find that the energetically lowest hK' interlayer exciton (blue-shaded) has the largest PL contribution. It consists of a direct zero-phonon peak at -295 and two smaller peaks (pink-shaded) at -310 and -345 meV stemming from indirect light emission driven by acoustic and optical phonons, respectively. Note that these peaks appear at the location $E_{hK'} \pm \Omega^{A/O}$, i.e. they are shifted by the phonon energy. We find that the hΛ interlayer exciton has a smaller direct contribution (green-shaded) reflecting its lower occupation compared to hK' states as well as a smaller phonon-sideband contribution (red-shaded). By increasing the temperature, the ILX occupation decreases, reducing their weight in PL spectra. The total PL spectra (blue line) is therefore asymmetric with a clear optical sideband indicated by an arrow. Furthermore, the sidebands from the acoustic spectrum leads to a slight shift in the maximum PL intensity, about 10 meV below the PL resonance. Finally, there is also a slight asymmetry at higher energies due to smaller hΛ interlayer exciton contribution.

For comparison, in MoSe$_2$ the hK exciton is the energetically lowest state[9–11,32]. As a result, the low-temperature PL spectrum is qualitatively different exhibiting only one peak at -346 meV stemming from the hK interlayer exciton, cf. Fig. 4(c). There are no signatures from the hK' and hΛ interlayer exciton due to their lower occupation, however a small phonon-sideband originating from the hK exciton is visible in the spectra (marked by an arrow). In the SI, we present results for a pentacene/MoS$_2$ heterostructure, where the larger separation between the inter- and intralayer excitons leads to a more dominant interlayer state in the PL spectrum. In this case, we also find the emergence of phonon sidebands at lower temperatures. Our predictions about interlayer excitons and the role of phonons are applicable to a larger class of TMD/organic heterostructures. In particular, these materials should facilitate interlayer exciton formation, through type-II band alignment and efficient charge transfer. This will ensure a significant interlayer exciton population and hence a strong optical signal compared to the much brighter intralayer excitons. The phonon sidebands will emerge given sufficiently strong exciton-phonon interactions. Heterostructures composed of MX2 (M= Mo, W X= S, Se) TMDs will certainly satisfy the latter requirement and should form interlayer excitons with polyacenes, such as pentacene, tetracene as well as their derivatives, through functionalisation of the aromatic rings. While the list of possible structures is vast, some notable examples where we expect interlayer excitons and sidebands to emerge are TMD/rubrene[62], TMD/TTF[63] and TMD/PTCDA[64] heterostructures all of which demonstrate efficient charge separation and type-II band alignment.

Theory-experiment comparison. To experimentally verify the theoretically predicted low temperature PL interlayer exciton signatures, we fabricated a high-quality WS$_2$/Tc heterostructure and collected its PL spectra over a broad temperature range (100-245 K). To prepare the heterostructure, a monolayer of WS$_2$ was exfoliated onto a silicon dioxide wafer (oxide thickness of 90 nm) from bulk WS$_2$. A 20 nm layer of Tc was then thermally evaporated onto the monolayer. Further information on sample preparation is included in the SI. We selectively excited WS$_2$ with 2.14 eV light to prevent the signal from interlayer excitons to become masked by Tc emission. Fig. 5(a) shows the measured temperature dependent PL of the heterostructure. At 245 K, the interlayer hK' exciton emits at 1.71 eV and its intensity significantly grows with decreasing temperature. This reflects the increasing occupation of the hK' excitonic state, which is in excellent agreement with our calculations, cf. Fig. 5(b). In the inset, we compare the experimental (red crosses) and theoretical (pink curve) evolution of the ILX intensity as a function of temperature. We normalize the ILX intensity to the value at 100 K. We find a good agreement between our theoretical model and experimental data, with a significant PL from the hK' exciton in the temperature range of 100-200 K. By performing a double-Gaussian fit, and taking the area under the curves, we are able to attribute the temperature evolution of the ILX peak to a change in exciton occupation N_μ, rather
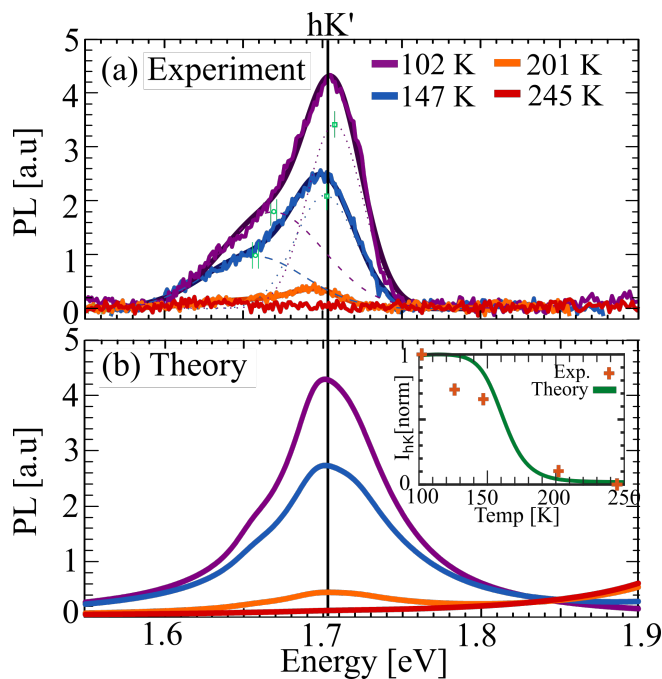

Figure 5. **Experiment-theory comparison.** (a) Temperature-dependent PL spectra (a) measured in experiment and (b) predicted from microscopic theory for WS$_2$/Tc on an SiO$_2$/Si substrate. Note that the theoretical spectra are shifted to align with the experimental hK' exciton peak. Raw data can be fitted to using two Gaussian peaks (dotted and dashed line), which we attribute to the direct PL and phonon-sidebands, respectively. Error bars for the energetic position of these Gaussian peaks are shown in green. Inset shows a quantitative comparison of the evolution of the intensity of the hK' resonance as a function of temperature, (normalised to the peak maximum). In (a) and in the inset, we removed contributions from the background PL in experiment to allow for a more accurate comparison.

than a broadening effect (see SI). Note that while we have the means to microscopically estimate the radiative and phonon-induced broadening of exciton peaks, broadening mechanisms in TMD-molecule heterostructures are currently not well understood, and our model underestimates the observed experimental broadening. Therefore, to better compare to experiment we extract values for the broadening from the experimental data and use a phenomenological model[7] to describe the temperature dependence in Fig. 5(b).

At around 100 K, we observe the increase in the intensity of a shoulder peak around 1.67 eV as indicated by the Gaussian fit (Fig. 5 (a)). This signature also appears in the theoretically calculated PL spectrum, cf. Fig 5(b) at 1.66 eV, and can be ascribed to a phonon sideband stemming from the indirect, phonon-assisted recombination of the hK' interlayer exciton states. In the theory, the sideband is red-shifted with respect to the position of the hK' resonance at 1.70 eV, reflecting the emission of an optical phonon[32]. At low temperatures, the signature of the phonon sideband increases relative to the zero-phonon peak due to the lower phonon-induced broadening. At temperatures above 200 K, this phonon sideband vanishes and is hardly visible in both the theory and experiment due to

the lower occupation of the hK' exciton and increased broadening. This experimental feature is consistent for different trials (see SI). The spectral profiles including peak positions and temperature dependence are all typical hallmarks of interlayer phonon-sidebands[65]. Furthermore, we have performed lifetime measurements at 102 K and 245 K, cf. the SI. Upon cooling to 102 K, the heterostructure's lifetime is considerably enhanced. The large increase in lifetime provides further evidence that at low temperature we indeed access ILX states.

In the SI, we show the temperature- as well as the pump fluence-dependence of the PL for an additional WS_2/Tc sample. We find excellent agreement for the temperature dependence between the two samples, with the PL interlayer exciton resonance clearly visible, decaying as the temperature increases with a pronounced sideband. This additional sample, in conjunction with previous studies[17] demonstrates the reproducibility of the interlayer exciton state in WS_2/Tc heterostructures.

The fluence-dependence further demonstrates the excitonic origin of the observed emission peak, as the linear-dependence of the exciton PL intensity with increasing pump-power is characteristic of excitons rather than trion states which saturate more rapidly. While PL saturation is predicted for TMD-TMD interlayer excitons[14], we predict that this occurs at much larger excitation strengths than probed in this work (c.f. supplementary information for a more detailed discussion). The absence of this state in respective monolayers, the energetic position far below the intralayer exciton, the temperature dependence, the fluence behaviour and longer lifetime all indicate that this state is indeed an interlayer state, which has been reproduced across multiple samples, both here, in the SI and in previous studies[17].

While we obtain an excellent qualitative agreement between theory and experiment, some quantitative discrepancies do exist. In particular, there is an increasing PL signal at higher energies above the hK' resonance in the experiment, while in theory the PL is strongly suppressed in this spectral region. This could be traced back to a particularly broad intralayer exciton resonance in the experiment that is expected to occur at about 2 eV (see supplementary information).

Interestingly, the peak position of the hK' interlayer exciton does not spectrally shift in the experiment. This suggests that the temperature-dependent Varshni energy shifts, arising from the thermal expansion of the crystal lattice[66], are negligible for interlayer excitons, justifying the omission of such effects in our theory. The suppressed Varshni shift could be explained by the involvement of the molecular lattice, which is expected to be less susceptible to thermal expansion when placed on a substrate such as WS_2. The latter is a fairly flat surface and hence the thermal expansion of the Tc will be frustrated due to fixation between the molecular layer and the WS_2[67]. Finally, the position of the observed phonon-sideband is slightly lower in energy than theoretically predicted (cf. arrows in Fig. 5). While we have fairly accurate estimates of the phonon dispersion for a pure TMD, phonon energies in a WS_2/Tc heterostructure might differ. A first principle calculation of the phonon dispersion for the TMD/Tc heterostructure is beyond the scope of this work.

In conclusion, we have presented a joint theory-experiment study on the optical response of interlayer excitons in a TMD/Tc heterostructure. We microscopically reveal the entire landscape of interlayer excitons living in both molecule and TMD layer and show their signatures in temperature-dependent PL spectra. In particular, we find both in experiment and theory a clear signature of interlayer excitons in PL spectra and show how their intensity can be boosted by variation in temperature. Furthermore, we show the appearance of an additional low-energy PL signature at temperatures around 100 K stemming from indirect phonon-assisted emission from interlayer exciton states. Our work provides new insights into the microscopic nature of interlayer excitons in TMD/molecule heterostructures and could guide future studies in the growing research field of technologically promising organic/inorganic heterostructures.

* joshua.thompson@physik.uni-marburg.de

[1] Geim, A. K.; Grigorieva, I. V. Van der Waals heterostructures. *Nature* **2013**, *499*, 419–425.

[2] Liu, Y.; Zhang, S.; He, J.; Wang, Z. M.; Liu, Z. Recent progress in the fabrication, properties, and devices of heterostructures based on 2D materials. *Nano-Micro Letters* **2019**, *11*, 1–24.

[3] Alexeev, E. M. et al. Resonantly hybridized excitons in moiré superlattices in van der Waals heterostructures. *Nature* **2019**, *567*, 81–86.

[4] Jin, C.; Regan, E. C.; Yan, A.; Utama, M. I. B.; Wang, D.; Zhao, S.; Qin, Y.; Yang, S.; Zheng, Z.; Shi, S.; Watanabe, K.; Taniguchi, T.; Tongay, S.; Zettl, A.; Wang, F. Observation of moiré excitons in WSe 2/WS 2 heterostructure superlattices. *Nature* **2019**, *567*, 76–80.

[5] Tran, K. X. et al. Evidence for moiré excitons in van der Waals heterostructures. *Nature* **2019**, *567*, 71–75.

[6] Merkl, P.; Mooshammer, F.; Steinleitner, P.; Girnghuber, A.; Lin, K.-Q.; Nagler, P.; Holler, J.; Schüller, C.; Lupton, J. M.; Korn, T.; Ovesen, S.; Brem, S.; Ermin, M.; Huber, R. Ultrafast transition between exciton phases in van der Waals heterostructures. *Nature materials* **2019**, *18*, 691–696.

[7] Brem, S.; Lin, K.-Q.; Gillen, R.; Bauer, J. M.; Maultzsch, J.; Lupton, J. M.; Malic, E. Hybridized intervalley moiré excitons and flat bands in twisted WSe 2 bilayers. *Nanoscale* **2020**, *12*, 11088–11094.

[8] Brem, S.; Linderälv, C.; Erhart, P.; Malic, E. Tunable Phases of Moiré Excitons in van der Waals Heterostructures. *Nano letters* **2020**, *20*, 8534–8540.

9 Deilmann, T.; Thygesen, K. S. Finite-momentum exciton landscape in mono-and bilayer transition metal dichalcogenides. *2D Materials* **2019**, *6*, 035003.

10 Malic, E.; Selig, M.; Feierabend, M.; Brem, S.; Christiansen, D.; Wendler, F.; Knorr, A.; Berghäuser, G. Dark excitons in transition metal dichalcogenides. *Physical Review Materials* **2018**, *2*, 014002.

11 Madéo, J.; Man, M. K.; Sahoo, C.; Campbell, M.; Pareek, V.; Wong, E. L.; Al-Mahboob, A.; Chan, N. S.; Karmakar, A.; Mariserla, B. M. K., et al. Directly visualizing the momentum-forbidden dark excitons and their dynamics in atomically thin semiconductors. *Science* **2020**, *370*, 1199–1204.

12 Wallauer, R.; Perea-Causin, R.; Munster, L.; Zajusch, S.; Brem, S.; Gudde, J.; Tanimura, K.; Lin, K.-Q.; Huber, R.; Malic, E., et al. Momentum-Resolved Observation of Exciton Formation Dynamics in Monolayer WS2. *Nano Letters* **2021**, *21*, 5867–5873.

13 Merkl, P.; Mooshammer, F.; Brem, S.; Girnghuber, A.; Lin, K.-Q.; Weigl, L.; Liebich, M.; Yong, C.-K.; Gillen, R.; Maultzsch, J., et al. Twist-tailoring Coulomb correlations in van der Waals homobilayers. *Nature communications* **2020**, *11*, 1–7.

14 Rivera, P.; Schaibley, J. R.; Jones, A. M.; Ross, J. S.; Wu, S.; Aivazian, G.; Klement, P.; Seyler, K.; Clark, G.; Ghimire, N. J., et al. Observation of long-lived interlayer excitons in monolayer MoSe 2–WSe 2 heterostructures. *Nature communications* **2015**, *6*, 1–6.

15 Hong, X.; Kim, J.; Shi, S.-F.; Zhang, Y.; Jin, C.; Sun, Y.; Tongay, S.; Wu, J.; Zhang, Y.; Wang, F. Ultrafast charge transfer in atomically thin MoS 2/WS 2 heterostructures. *Nature nanotechnology* **2014**, *9*, 682.

16 Kunstmann, J.; Mooshammer, F.; Nagler, P.; Chaves, A.; Stein, F.; Paradiso, N.; Plechinger, G.; Strunk, C.; Schüller, C.; Seifert, G., et al. Momentum-space indirect interlayer excitons in transition-metal dichalcogenide van der Waals heterostructures. *Nature Physics* **2018**, *14*, 801–805.

17 Zhu, T.; Yuan, L.; Zhao, Y.; Zhou, M.; Wan, Y.; Mei, J.; Huang, L. Highly mobile charge-transfer excitons in two-dimensional WS2/tetracene heterostructures. *Science Advances* **2018**, *4*, 3104.

18 Li, H.; Dong, Z.; Zhang, Y.; Li, L.; Wang, Z.; Wang, C.; Zhang, K.; Zhang, H. Recent progress and strategies in photodetectors based on 2D inorganic/organic heterostructures. *2D Materials* **2020**, *8*, 012001.

19 Gobbi, M.; Orgiu, E.; Samorì, P. When 2D materials meet molecules: opportunities and challenges of hybrid organic/inorganic van der Waals heterostructures. *Advanced Materials* **2018**, *30*, 1706103.

20 Lee, G.-H.; Lee, C.-H.; Van Der Zande, A. M.; Han, M.; Cui, X.; Arefe, G.; Nuckolls, C.; Heinz, T. F.; Hone, J.; Kim, P. Heterostructures based on inorganic and organic van der Waals systems. *Apl Materials* **2014**, *2*, 092511.

21 Costa, J. C.; Taveira, R. J.; Lima, C. F.; Mendes, A.; Santos, L. M. Optical band gaps of organic semiconductor materials. *Optical Materials* **2016**, *58*, 51–60.

22 Kachel, S. R.; Dombrowski, P.-M.; Breuer, T.; Gottfried, J. M.; Witte, G. Engineering of TMDC–OSC hybrid interfaces: the thermodynamics of unitary and mixed acene monolayers on MoS 2. *Chemical science* **2021**, *12*, 2575–2585.

23 Huang, Y. L.; Zheng, Y. J.; Song, Z.; Chi, D.; Wee, A. T.; Quek, S. Y. The organic–2D transition metal dichalcogenide heterointerface. *Chemical Society Reviews* **2018**, *47*, 3241–3264.

24 Bettis Homan, S.; Sangwan, V. K.; Balla, I.; Bergeron, H.; Weiss, E. A.; Hersam, M. C. Ultrafast exciton dissociation and long-lived charge separation in a photovoltaic pentacene–MoS2

van der Waals heterojunction. *Nano letters* **2017**, *17*, 164–169.

25 Jariwala, D.; Sangwan, V. K.; Late, D. J.; Johns, J. E.; Dravid, V. P.; Marks, T. J.; Lauhon, L. J.; Hersam, M. C. Band-like transport in high mobility unencapsulated single-layer MoS2 transistors. *Applied Physics Letters* **2013**, *102*, 173107.

26 Wu, T. C.; Thompson, N. J.; Congreve, D. N.; Hontz, E.; Yost, S. R.; Van Voorhis, T.; Baldo, M. A. Singlet fission efficiency in tetracene-based organic solar cells. *Applied Physics Letters* **2014**, *104*, 193901.

27 Bischof, D.; Tripp, M. W.; Hofmann, P. E.; Ip, C.-H.; Ivlev, S. I.; Gerhard, M.; Koert, U.; Witte, G. Regioselective Fluorination of Acenes: Tailoring of Molecular Electronic Levels and Solid-State Properties. *Chemistry–A European Journal* **2022**, e202103653.

28 Ovesen, S.; Brem, S.; Linderälv, C.; Kuisma, M.; Korn, T.; Erhart, P.; Selig, M.; Malic, E. Interlayer exciton dynamics in van der Waals heterostructures. *Communications Physics* **2019**, *2*, 1–8.

29 Haug, H.; Koch, S. W. *Quantum theory of the optical and electronic properties of semiconductors*; World Scientific Publishing Company, 2009.

30 Kira, M.; Koch, S. Many-body correlations and excitonic effects in semiconductor spectroscopy. *Progress in Quantum Electronics* **2006**, *30*, 155 – 296.

31 Brem, S.; Ekman, A.; Christiansen, D.; Katsch, F.; Selig, M.; Robert, C.; Marie, X.; Urbaszek, B.; Knorr, A.; Malic, E. Phonon-assisted photoluminescence from indirect excitons in monolayers of transition-metal dichalcogenides. *Nano Letters* **2020**, *20*, 2849–2856.

32 Selig, M.; Berghäuser, G.; Richter, M.; Bratschitsch, R.; Knorr, A.; Malic, E. Dark and bright exciton formation, thermalization, and photoluminescence in monolayer transition metal dichalcogenides. *2D Materials* **2018**, *5*, 035017.

33 Park, H. J.; Park, C.-J.; Kim, J. Y.; Kim, M. S.; Kim, J.; Joo, J. Hybrid characteristics of MoS2 monolayer with organic semiconducting tetracene and application to anti-ambipolar field effect transistor. *ACS applied materials & interfaces* **2018**, *10*, 32556–32566.

34 Amsterdam, S. H.; LaMountain, T.; Stanev, T. K.; Sangwan, V. K.; López-Arteaga, R.; Padgaonkar, S.; Watanabe, K.; Taniguchi, T.; Weiss, E. A.; Marks, T. J.; Hersam, M. C.; Stern, N. P. Tailoring the Optical Response of Pentacene Thin Films via Templated Growth on Hexagonal Boron Nitride. *The Journal of Physical Chemistry Letters* **2020**, *12*, 26–31.

35 Rotter, P.; Lechner, B. A.; Morherr, A.; Chisnall, D. M.; Ward, D. J.; Jardine, A. P.; Ellis, J.; Allison, W.; Eckhardt, B.; Witte, G. Coupling between diffusion and orientation of pentacene molecules on an organic surface. *Nature materials* **2016**, *15*, 397–400.

36 Witte, G.; Wöll, C. Growth of aromatic molecules on solid substrates for applications in organic electronics. *Journal of Materials Research* **2004**, *19*, 1889–1916.

37 El Helou, M.; Medenbach, O.; Witte, G. Rubrene microcrystals: A route to investigate surface morphology and bulk anisotropies of organic semiconductors. *Crystal growth & design* **2010**, *10*, 3496–3501.

38 Käfer, D.; Witte, G. Evolution of pentacene films on Ag (1 1 1): Growth beyond the first monolayer. *Chemical physics letters* **2007**, *442*, 376–383.

39 Niederhausen, J.; MacQueen, R. W.; Lips, K.; Aldahhak, H.; Schmidt, W. G.; Gerstmann, U. Tetracene ultrathin film growth on hydrogen-passivated silicon. *Langmuir* **2020**, *36*, 9099–9113.

40 Breuer, T.; Maßmeyer, T.; Mänz, A.; Zoerb, S.; Harbrecht, B.; Witte, G. Structure of van der Waals bound hybrids of organic semiconductors and transition metal dichalcogenides: the case of

acene films on MoS2. *physica status solidi (RRL)–Rapid Research Letters* **2016**, *10*, 905–910.

[41] Gavrila, G.; Mendez, H.; Kampen, T.; Zahn, D.; Vyalikh, D.; Braun, W. Energy band dispersion in well ordered N, N-dimethyl-3, 4, 9, 10-perylenetetracarboxylic diimide films. *Applied physics letters* **2004**, *85*, 4657–4659.

[42] Fedorov, I. A. First-principles study of band structures of anthracene and tetracene under pressure. *Materials Chemistry and Physics* **2017**, *199*, 173–178.

[43] Cocchi, C.; Breuer, T.; Witte, G.; Draxl, C. Polarized absorbance and Davydov splitting in bulk and thin-film pentacene polymorphs. *Physical Chemistry Chemical Physics* **2018**, *20*, 29724–29736.

[44] Doi, K.; Yoshida, K.; Nakano, H.; Tachibana, A.; Tanabe, T.; Kojima, Y.; Okazaki, K. Ab initio calculation of electron effective masses in solid pentacene. *Journal of applied physics* **2005**, *98*, 113709.

[45] Hu, P.; Li, H.; Li, Y.; Jiang, H.; Kloc, C. Single-crystal growth, structures, charge transfer and transport properties of anthracene-F 4 TCNQ and tetracene-F 4 TCNQ charge-transfer compounds. *CrystEngComm* **2017**, *19*, 618–624.

[46] Ma, J.; Amsalem, P.; Schultz, T.; Shin, D.; Xu, X.; Koch, N. Energy Level Alignment at the C60/Monolayer-WS2 Interface on Insulating and Conductive Substrates. *Advanced Electronic Materials* **2021**, *7*, 2100425.

[47] Berghäuser, G.; Steinleitner, P.; Merkl, P.; Huber, R.; Knorr, A.; Malic, E. Mapping of the dark exciton landscape in transition metal dichalcogenides. *Physical Review B* **2018**, *98*, 020301.

[48] Rosati, R.; Schmidt, R.; Brem, S.; Perea-Causín, R.; Niehues, I.; Kern, J.; Preuß, J. A.; Schneider, R.; Michaelis de Vasconcellos, S.; Bratschitsch, R., et al. Dark exciton anti-funneling in atomically thin semiconductors. *Nature Communications* **2021**, *12*, 1–7.

[49] Berghäuser, G.; Malic, E. Analytical approach to excitonic properties of MoS_2. *Phys. Rev. B* **2014**, *89*, 125309.

[50] Brem, S.; Selig, M.; Berghaeuser, G.; Malic, E. Exciton Relaxation Cascade in two-dimensional Transition Metal Dichalcogenides. *Scientific reports* **2018**, *8*, 8238.

[51] Kormanyos, A.; Burkard, G.; Gmitra, M.; Fabian, J.; Zolyomi, V.; Drummond, N. D.; Falko, V. k · p theory for two-dimensional transition metal dichalcogenide semiconductors. *2D Materials* **2015**, *2*, 022001.

[52] Zhang, C.; Gong, C.; Nie, Y.; Min, K.-A.; Liang, C.; Oh, Y. J.; Zhang, H.; Wang, W.; Hong, S.; Colombo, L., et al. Systematic study of electronic structure and band alignment of monolayer transition metal dichalcogenides in Van der Waals heterostructures. *2D Materials* **2016**, *4*, 015026.

[53] Hagel, J.; Brem, S.; Linderälv, C.; Erhart, P.; Malic, E. Exciton landscape in van der Waals heterostructures. *arXiv preprint arXiv: 2109.10746* **2021**,

[54] Chernikov, A.; Berkelbach, T. C.; Hill, H. M.; Rigosi, A.; Li, Y.; Aslan, O. B.; Reichman, D. R.; Hybertsen, M. S.; Heinz, T. F. Exciton Binding Energy and Nonhydrogenic Rydberg Series in Monolayer WS$_2$. *Phys. Rev. Lett.* **2014**, *113*, 076802.

[55] Arora, A.; Koperski, M.; Nogajewski, K.; Marcus, J.; Faugeras, C.; Potemski, M. Excitonic resonances in thin films of WSe 2: from monolayer to bulk material. *Nanoscale* **2015**, *7*, 10421–10429.

[56] Mueller, T.; Malic, E. Exciton physics and device application of two-dimensional transition metal dichalcogenide semiconductors. *npj 2D Materials and Applications* **2018**, *2*, 1–12.

[57] Feldtmann, T.; Kira, M.; Koch, S. W. Phonon sidebands in semiconductor luminescence. *physica status solidi (b)* **2009**, *246*, 332–336.

[58] Chernikov, A.; Bornwasser, V.; Koch, M.; Chatterjee, S.; Böttge, C.; Feldtmann, T.; Kira, M.; Koch, S.; Wassner, T.; Lautenschläger, S., et al. Phonon-assisted luminescence of polar semiconductors: Fröhlich coupling versus deformation-potential scattering. *Physical Review B* **2012**, *85*, 035201.

[59] Erkensten, D.; Brem, S.; Wagner, K.; Gillen, R.; Perea-Causín, R.; Ziegler, J. D.; Taniguchi, T.; Watanabe, K.; Maultzsch, J.; Chernikov, A.; Malic, E. Dark exciton-exciton annihilation in monolayer WSe 2. *Physical Review B* **2021**, *104*, L241406.

[60] Axt, V.; Victor, K.; Stahl, A. Influence of a phonon bath on the hierarchy of electronic densities in an optically excited semiconductor. *Physical Review B* **1996**, *53*, 7244.

[61] Selig, M.; Berghäuser, G.; Raja, A.; Nagler, P.; Schüller, C.; Heinz, T. F.; Korn, T.; Chernikov, A.; Malic, E.; Knorr, A. Excitonic linewidth and coherence lifetime in monolayer transition metal dichalcogenides. *Nature communications* **2016**, *7*, 13279.

[62] Park, C.-J.; Park, H. J.; Lee, J. Y.; Kim, J.; Lee, C.-H.; Joo, J. Photovoltaic field-effect transistors using a MoS2 and organic rubrene van der Waals hybrid. *ACS applied materials & interfaces* **2018**, *10*, 29848–29856.

[63] Cai, Y.; Zhou, H.; Zhang, G.; Zhang, Y.-W. Modulating carrier density and transport properties of MoS2 by organic molecular doping and defect engineering. *Chemistry of Materials* **2016**, *28*, 8611–8621.

[64] Liu, X.; Gu, J.; Ding, K.; Fan, D.; Hu, X.; Tseng, Y.-W.; Lee, Y.-H.; Menon, V.; Forrest, S. R. Photoresponse of an organic semiconductor/two-dimensional transition metal dichalcogenide heterojunction. *Nano letters* **2017**, *17*, 3176–3181.

[65] Rosati, R.; Wagner, K.; Brem, S.; Perea-Causín, R.; Wietek, E.; Zipfel, J.; Ziegler, J. D.; Selig, M.; Taniguchi, T.; Watanabe, K.; Knorr, A.; Chernikov, A.; Malic, E. Temporal Evolution of Low-Temperature Phonon Sidebands in Transition Metal Dichalcogenides. *ACS Photonics* **2020**, *7*, 2756–2764.

[66] Varshni, Y. P. Temperature dependence of the energy gap in semiconductors. *physica* **1967**, *34*, 149–154.

[67] von Helden, L.; Breuer, T.; Witte, G. Anisotropic thermal expansion in pentacene and perfluoropentacene: Effects of molecular packing motif and fixation at the interface. *Applied Physics Letters* **2017**, *110*, 141904.